Redox responsive nanoparticle encapsulating black phosphorus quantum dots for cancer theranostics

Haolin Chen [a,1], Zhiming Liu [b,1], Bo Wei [c], Jun Huang [a], Xinru You [a], Jingyang Zhang [a], Zhiling Yuan [c], Zhilie Tang [c], Zhouyi Guo [b], Jun Wu [a,*]

[a] *Key Laboratory of Sensing Technology and Biomedical Instrument of Guangdong Province, School of Biomedical Engineering, Sun Yat-sen University, Guangzhou, 510006, China*
[b] *MOE Key Laboratory of Laser Life Science & SATCM Third Grade Laboratory of Chinese Medicine and Photonics Technology, College of Biophotonics, South China Normal University, Guangzhou, 510631, China*
[c] *School of Physics and Telecommunication Engineering, South China Normal University, Guangzhou, 510006, China*

ARTICLE INFO

ABSTRACT

Effective cancer treatment puts high demands for cancer theranostics. For cancer diagnostics, optical coherence tomography (OCT) technology (including photothermal optical coherence tomography (PT-OCT)) has been widely investigated since it induces changes in optical phase transitions in tissue through environmental changes (such as temperature change for PT-OCT). In this report, redox responsive nanoparticle encapsulating black phosphorus quantum dots was developed as a robust PT-OCT agent. Briefly, black phosphorus quantum dots (BPQDs) are incorporated into cysteine-based poly-(disulfide amide) (Cys-PDSA) to form stable and biodegradable nanoagent. The excellent photothermal feature allows BPQD/Cys-PDSA nanoparticles (NPs) as a novel contrast agent for high-resolution PT-OCT bioimaging. The Cys-PDSA can rapidly respond to glutathione and effectively release BPQDs and drugs *in vitro* and *in vivo*. And the obtained NPs exhibit excellent near-infrared (NIR) photothermal transduction efficiency and drug delivery capacity that can serve as novel therapeutic platform, with very low chemo drug dosage and side effects. Both of the polymer and BPQD are degradable, indicating this platform is a rare PT-OCT agent that is completely biodegradable. Overall, our research highlights a biodegradable and biocompatible black phosphorus-based nanoagent for both cancer diagnosis and therapy.

1. Introduction

For cancer diagnosis, noninvasive imaging techniques have attracted enormous research interests [1–3]. Among them, optical coherence tomography (OCT) is a high-speed, noninvasive and high-resolution three-dimensional imaging technique based on the interference of low-coherent light, by which the microstructure of biological tissue can be evaluated at the cellular and sub-cellular level with the micron resolution [4–6]. Recently, photothermal optical coherence tomography (PT-OCT) has been developed as a variant of OCT technology that induces changes in optical phase transitions in tissue through temperature changes under additional laser irradiation [7–11]. However, the current contrast agents for PT-OCT, such as gold-based contrast agents, has some biosafety concerns [12,13]. Therefore, novel PT-OCT probes with required biocompatibility and biodegradability are of

great interests. In this study, we designed and developed black phosphorus quantum dots (BPQDs) based nanoagent as novel PT-OCT probe and drug carrier for effective cancer theranostics. Black phosphorus (BP), a new kind of two-dimensional material, has a layer-dependent band gap between 0.3 and 2.0 eV, making it more versatile for electronic and optoelectronic applications than graphene [14–16]. Recently, BPQDs have served as biocompatible photo-responsive nanoagents for photothermal and photodynamic cancer therapy due to their broad light absorption across the ultraviolet and near-infrared regions [17–20]. Specifically, BP or BPQDs could be easily degraded by oxygen and water, resulting better biosafety [21–24]. However, this characteristics caused BPQDs suffer from rapid renal excretion and overquick degradation in the blood circulation, which limit its biomedical applications. Therefore, smart platforms that could enhance the stability of BPQDs are highly desired [25–27].
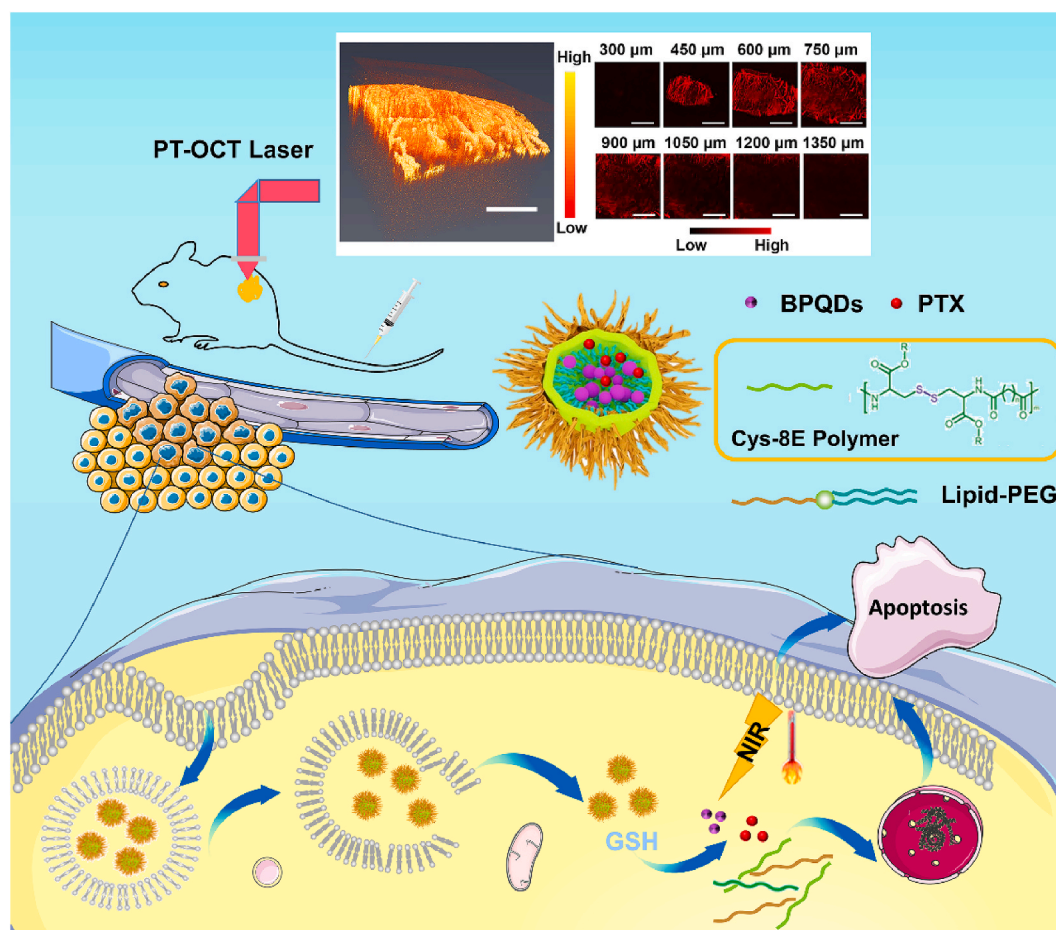
Scheme 1. Schematic illustration of black phosphorus-based theranostic platform and its therapeutic application.

In this study, we designed and developed hydrophobic cysteine-based poly-(disulfide amide) (Cys-PDSA) polymers as BPQDs nano-carrier that can respond to glutathione (GSH) via disulfide-mediated reduction. BPQDs can be loaded into Cys-8E polymer by the nanopre-cipitation method to produce ~150 nm BPQD/Cys-8E NPs (Scheme 1), thereby acquiring high stability of BPQDs in aqueous dispersions/blood and further endows the nanostructures with GSH-responsive feature for nanotheranostic application. By means of the photothermal effect, PT-OCT cancer imaging is carried out using BP based materials as contrast agents. Finally, the anticancer drug paclitaxel (PTX) was loaded into the nanoparticles to achieve combined chemotherapy and photothermal cancer therapy.

2. Materials and methods

2.1. Materials

The BP crystals were purchased from Nanjing XFNANO Materials and stored in a dark Argon glovebox. Lipid-PEG (1,2-distearoyl-*sn*-gly-cero-3-phosphoethanolamine poly (ethylene glycol) 2000 (DSPE-PEG 2000)) was bought from Avanti Polar Lipids. Paclitaxel (PTX) was purchased from LC laboratories. The PBS (pH 7.4), foetal bovine serum, RPMI-1640, trypsin-EDTA, Calcein AM and propidium iodide (PI) were obtained from Gibco Life Technologies. *N*-methyl-2-pyrrolidone (NMP) (99.5%, anhydrous), DMSO and dithiothreitol (DTT) were supplied by Aladdin Reagents. The NIR fluorescence dye 1,1′-dioctadecyl-3,3,3′,3′-tetramethylindotricar-bocyanine iodide (DiR), Coumarin 6 (C6), 1,1′-dioctadecyl-3,3,3′,3′-tetramethylindocarbocyanine perchlorate (DiI), were all purchased from Thermo Fisher Scientific. All the chemicals used in this study were analytical reagent grade and used without

further purification. Ultrapure water (18.25 MΩ cm, 25 °C) was used to prepare the solutions.

2.2. Characterization

Transmission electron microscope (TEM) images were obtained using transmission electron microscope (Tecnai G2 Spirit, FEI, USA) operated at 120 kV. HRTEM images and HAADF images were recorded by using transmission electron microscope (Tecnai G2 F30, FEI, USA) operated at 300 kV. UV–vis absorption spectra were recorded using a UV–Vis spectrometer (DU730, Beckman, USA). Raman spectra were performed on a Renishaw inVia microspectrometer (Derbyshire, England) under laser excitation at 785 nm. The zeta potential and size distribution measurements were carried out on a Malvern Zetasizer Nano ZS system (Malvern Instruments, UK) at the temperature of 25 °C and with a scattering angle of 90°. Confocal fluorescence microscopic images were obtained using a laser scanning confocal microscopy (FV 3000, Olympus, Japan).

2.3. Synthesis of Cys-PDSA polymers

The preparation of Cys-PDSA polymers were described previously [33]. The details of one-step polycondensation reaction were carried out as follows: (H-Cys-OMe)$_2$·2HCl (10 mmol) and triethylamine (15 mmol) were dissolved in DMSO (20 mL), cautiously added, the dichloride of fatty acid (10 mmol) DMSO solution (10 mL). The solution was stirred for 15 min to get a homogeneous mixture, then precipitated twice with 250 mL of ice-cold diethyl ether, and dried under vacuum to obtain a white or yellow powder.

2.4. Synthesis of BPQDs

The BPQDs were prepared from bulk BP crystals by a simple liquid exfoliation technique described in the literature [31]. In brief, 30 mg of the bulk BP powders were dispersed in 30 mL of NMP and sonicated with an ultrasonic cell disruption system for 6 h with the ultrasound probe working for 5 s with an interval of 4 s using a power of 750 W. The dispersion was sonicated overnight in an ice bath at a power of 300 W. The resulting dispersion was centrifuged for 20 min at 7000 rpm. and the supernatant containing the BPQDs was decanted gently. The supernatant was then centrifuged at 13,000 rpm for 45 min to remove NMP. The precipitate was finally rinsed repeatedly with DMSO and resuspended in DMSO for further use.

2.5. Preparation of BPQD/Cys-8E nanoparticles

The BPQD/Cys-8E nanoparticles were prepared via nanoprecipitation method. In brief, 80 μL of the BPQDs suspension in DMSO (1 mg/mL), 20 μL of Cys-8E polymer (20 mg/mL) and 20 μL of DSPE-PEG (20 mg/mL) were dissolved in DMSO to form a homogenous solution. The mixture was dropwise added to the water (4 mL) under vigorous stirring (1200 rpm). Then the NP dispersion was transferred to an Amicon Ultra-15 Centrifugal Filter (MWCO 100 KDa, Millipore) and purified by centrifugation 3 times for further use. The particle size and distribution were measured by dynamic light scattering, and the surface zeta potential was measured and recorded as the average of three measurements.

2.6. Evaluation of the photothermal effect and photothermal stability of nanoparticles

The photothermal effect of BPQD/Cys-8E NPs induced by NIR laser irradiation was investigated by monitoring the temperature changes of various concentrations of BPQD/Cys-8E NPs (BPQDs content: 0, 20, 40, 80 μg/mL aqueous solution). The sample was fixed on an iron pedestal and then irradiated with a continuous-wave diode NIR laser (808 nm, 2 W/cm^2). Real-time thermal imaging and temperature change in the sample was recorded by an infrared thermal camera (Fluke Ti 200, Fluke Corp, Washington, USA). The BPQDs and the BPQD/Cys-8E NPs with the concentration of BPQDs were dispersed in neutral PBS (10 μg/mL) and water (20 μg/mL), respectively. The samples were kept in closed sample vials and maintained at 37 °C. Degradation of the BPQDs and BPQD/Cys-8E NPs were evaluated by the temperature change after 808 nm laser 2 W/cm^2 illumination for 10 min at scheduled time by the method mentioned above. The photostability of BPQD/Cys-8E NPs was tested for 5 cycles of irradiating and cooling processes.

2.7. Preparation of fluorescent dye-loaded nanoparticles

Dil-loaded BPQD/Cys-8E NPs, C6-loaded BPQD/Cys-8E NPs and DiR-loaded BPQD/Cys-8E NPs were prepared by mixing predetermined amounts of Cys-8E polymer, BPQDs and dye in DMSO, then following the nanoprecipitation procedure mentioned above.

2.8. Drug loading and release

BPQD/Cys-8E/PTX NPs were fabricated similar to the BPQD/Cys-8E NPs the previously described. In brief, BPQDs (1 mg/mL), Cys-8E polymer (20 mg/mL), PTX (20 mg/mL) and DSPE-PEG 2000 (20 mg/mL) with different proportions were dissolved in DMSO to form a homogenous solution. Then, the oil phase mixture was dropwise added to the water (4 mL) under vigorous stirring (1200 rpm). Then the dispersion was purified by using Amicon Ultra-15 Centrifugal Filter (MWCO 100 KDa, Millipore). The encapsulation efficiency (EE) and drug loading efficiency (DL) of PTX or BPQDs in BPQD/Cys-8E/PTX were determined by high-performance liquid chromatography (HPLC,

Agilent, USA) and inductively coupled plasma mass spectrometry, respectively. The mobile phase were water and acetonitrile (35:65) and at a flow rate of 1 mL/min (λ_{max} = 230 nm). The sample injection volume is 10 μL. The drug loading efficiency and encapsulation efficiency were calculated formulas were as follows:

$$EE = \frac{\text{Weight of encapsulated drug}}{\text{Weight of initial drug added}} \times 100\% \tag{1}$$

$$DL = \frac{\text{Weight of encapsulated drug}}{\text{Weight of NPs}} \times 100\% \tag{2}$$

To study the release behavior of PTX, the BPQD/Cys-8E/PTX NPs suspension was added into dialysis bag and dialyzed in 29 mL release media of 0, 1 or 10 mM DTT concentration at pH 7.4, followed by shaking at 37 °C with a speed of 100 rpm. At predetermined time points, 1 mL of the release medium was harvested and supplemented with the same amount of fresh dissolution medium. The amount of PTX released was determined by HPLC (λ_{max} = 230 nm) as above mentioned.

2.9. Cell viability

The HepG2 human liver hepatocellular carcinoma cells, H1650 human lung cancer cells, NIH-3T3 cells and murine breast cancer 4T1 cells were seeded in a 96-well plate (5 $\times$ 10^3 cells/well) filled with DMEM/RPMI-1640 medium supplemented with 10% fetal bovine serum, and 1% penicillin and streptomycin. The cells were cultured in humid chamber at a constant temperature of 37 °C with 5% CO$_2$. After 24 h of initial cell incubation, the medium was replaced with 100 μL of fresh medium containing BPQD/Cys-8E with concentrations of 0, 2, 5, 10, 20, 50, 100 μg/mL, respectively. Each sample was set for six multiple holes. After 24 h of co-incubation, CCK-8 assay was conducted. The absorbance was measured by a microplate Reader (Bio-tex, ELx 800, USA) at a wavelength of 450 nm.

The cell viability was normalized to the control group and was calculated by Eq. (3).

$$\text{Cell viability} = \frac{A_T}{A_C} \times 100\% \tag{3}$$

where A_T is the mean absorbance of treatment group and A_C is the mean absorbance of control group without treated with nanoparticles.

2.10. Confocal laser scanning microscope (CLSM)

HepG2 cells were seeded in disc at a density of 1 $\times$ 10^5 cells and incubated overnight to allow cell attachment. Subsequently, the Dil-loaded nanoparticles at a Dil dose of 5 μg/mL dispersed in RPMI-1640 medium were added and the cells were allowed to incubate for another 0.5 h, 1 h, 2 h, 4 h. Then, the medium containing excess nanoparticles was removed and subsequently washing with ice cold PBS (pH 7.4) solution several times. Next, the nuclei were stained with Hoechst 33,342 (5 μg/mL) for 10 min and followed by stained with endosomes with Lysotracker Green (100 nM) for 10 min. Subsequently, cells were fixed using neutral formalin for 10 min. Subsequently, the cells were kept in PBS and viewed under CLSM (FV3000, Olympus, Japan).

2.11. In vitro synergistic therapy

For the evaluation of the therapeutic effects of cancer, HepG2 and 4T1 cells were exposed to various concentrations of free PTX, BPQD/Cys-8E, BPQD/Cys-8E/PTX for 4 h, respectively. Then were or were not irradiated with a laser (808 nm, 2 W/cm^2) for 3 min. After incubation for another 24 h, CCK-8 assays were used to evaluate the cell viability. For the cell apoptosis experiments by flow cytometry, briefly, HepG2 cells with a density of 1 $\times$ 10^5 per well were seeded in a 24-well plate for overnight, and the groups were set (control, laser, PTX, BPQD/Cys-8E + laser, BPQD/Cys-8E/PTX + laser) with the equal concentration

of PTX was 5 μg/mL and internal BPQDs concentration was 23.75 μg/mL. After being irradiated with a laser (808 nm, 2 W/cm^2, 3 min) for another 12 h and 24 h incubation, the resulting cells were labeled with Annexin V-FITC/PI according to the protocol of Dead Cell Apoptosis Kit (Multisciences Biotech Co,. Ltd, Hangzhou, China) and analyzed via flow cytometry. Fluorescence images were also carried out to analyze the synergistic effects of BPQD/Cys-8E/PTX mediated photothermal combination therapy *in vitro*. HepG2 cells with a density of 1 × 10^5 were plated per well in 6-well plates, and groups settings were consistent with apoptosis flow cytometric detection. The laser exposure groups were irradiated with a laser (808 nm, 2 W/cm^2) for 10 min and incubated at 37 °C for an additional 4 h, then co-stained with calcein AM and propidium iodide (PI) for 30 min. The fluorescent pictures of the cells were taken with a fluorescence microscope (IX71, Olympus, Japan).

2.12. In vivo antitumor effect

Female BALB/c mice were purchased from laboratory animal center of Sun Yat-Sen University and were used under the guidelines approved by the Sun Yat-Sen University Laboratory Animal Center. 2 × 10^6 4T1 cells suspended in 100 μL PBS were subcutaneously injected into the right back of each female BALB/c mouse. The mice bearing 4T1 tumors were treated when the tumor volume reached ~150 mm^3. The 4T1 tumors bearing mice were randomly divided into 6 groups (n = 6 per group), minimizing the differences of weights and tumor sizes among groups. The mice were then tail intravenously injected with 100 μL PTX, BPQDs, BPQD/Cys-8E, BPQD/Cys-8E/PTX for the groups as follow: PBS (control, Group I), laser (Group II), PTX (Group III), BPQDs + laser (Group IV), BPQD/Cys-8E + laser (Group V), BPQD/Cys-8E/PTX + laser (Group VI). 100 μL of saline containing PTX (1 mg/kg), BPQDs (5 mg/kg), BPQD/Cys-8E (BPQDs concentration was 5 mg/kg), BPQD/Cys-8E/PTX (BPQD concentration was 5 mg/kg, PTX concentration was 1 mg/kg) was injected into mice intravenously. For Group I and Group II, mice were treated with the same volume of PBS. After 24 h, the laser treated mice were irradiated by an 808 nm NIR laser with a power density of 2 W/cm^2 for 3 min. The local temperature change of the mice was monitored during the irradiation using Thermal infrared imaging camera simultaneously. The tumors were collected from the BALB/c mice of each group after 24 h laser treatment. The individual tumors were fixed in 4% paraformaldehyde, embedded in paraffin, sectioned at 5 μm and stained using the TUNEL technique and H&E staining at the same time. The experimental procedures were in accordance with the manufacturer's instructions. For other mice, the dimension of tumor volume with calipers and body weight were measured every other day. The volume of tumors were calculated as following formula:

$$V = \frac{\text{tumor length} \times \text{tumor width}^2}{2} \qquad (4)$$

Relative tumor volumes were calculated as V/V_0 (where V_0 is the tumor volume when the treatment was started).

2.13. Biodistribution of nanoparticles by live imaging

Therefore, to study the *in vivo* behavior of the BPQD/Cys-8E NPs, DiR, a commonly used NIR fluorescent dye, was entrapped into the nanoparticles to label the BPQD/Cys-8E by using the nanoprecipitation method mentioned above. The BALB/c mice bearing 4T1 breast tumors assigned to two groups with three in each group. To observe the biodistribution of free DiR, DiR-labeled BPQD/Cys-8E NPs with a DiR dose of 0.5 mg/kg via the tail vein, and examined by a fluorescence imaging system (Xenogen IVIS-Spectrum, USA) at 2 h, 4 h, 8 h, 12 h, 24 h, 48 h post injection. The mice injected free DiR with an equivalent DiR-labeled BPQD/Cys-8E dose were set as control. At the final time, the mice

were sacrificed and major organs (heart, liver, spleen, lung, kidney, stomach, intestine, brain) were harvested and imaged.

2.14. Photothermal optical coherence tomography

All *in vitro* phantom and *in vivo* mouse imaging experiments were performed using a PT-OCT imaging system as illustrated in Fig. 3a, which combines new scanning methods and imaging principles on the basis of frequency-domain OCT systems, providing an axial resolution of 13.8 μm in air. The PT-OCT imaging system was equipped superluminescent diode (SLD) with a central wavelength of 1310 nm and a bandwidth of 58 nm as an OCT light source. The light from the SLD was coupled by 50/50 fiber coupler and split the light into reference arm and an object arm. A pump laser beam with a wavelength of 532 nm with an output power of ~20 mW used as the excitation light to photothermally excite the sample. The light of reference arm was reflected from a stationary mirror back to the broadband coupler. The lights from the SLD split by the 2 × 2 fiber coupler and the pump laser beams were combined in the sample arm with two dichroic mirrors, and an XY pair of scanning galvanometer system was used to laterally scan the sample. The light reflected from the reference arm and object arm was collected into the fiber coupler for interferometry. The output interference light was collimated into parallel light through a lens, then divided by the spectro-grating (1145 lines/mm, f = 50 mm, 1004–2, Thorlabs) and collected by a linear array CCD (SU1024-LDH2, Goodrich). A personal computer was used to control the data acquisition process, such as controlling the acquisition of the camera and the square wave excitation of the pump laser.

In vitro PT-OCT imaging measurements of BPQD/Cys-8E NPs with different BPQDs concentrations (0, 6.25, 12.5, 25, 50, 100 μg/mL) of agars were performed on the PT-OCT imaging system. For *in vivo* PT-OCT studies, BALB/c mice bearing subcutaneous tumors was injected with Cys-8E encapsulated BPQD NPs (1 mg/mL, 80 μL) via the tail vein. In-situ common OCT and PT-OCT images were acquired at 8 h, 12 h, 24 h, 48 h post injection using the PT-OCT imaging system at a wavelength of 532 nm. At the time point, three mice were sacrificed and their tumors were imaged with the PT-OCT system. BALB/c mice bearing 4T1 tumors without injected BPQD/Cys-8E NPs is set as control.

2.15. In vivo toxicity assessment

Body weights of animals were monitored every other day. Body weight change was defined as the relative body weight normalized to their initial weight. For blood analysis and histological examination, the animals were sacrificed 18 days after treatment, and the blood samples and major organs including heart, liver, spleen, lung and kidney were harvested. All the blood samples were collected for serum chemistry analysis and parameters (alanine transaminase (ALT), aspartate transaminase (AST), globulin (GLB), total protein (TP), albumin/globin ratio (A/G), total bilirubin (TBIL), blood urea nitrogen (BUN), creatinine (CREA) and albumin (ALB) were measured using Automatic Biochemical Analyzer (UniCel DxC 8008 Synchron Clinical System, Beckman Coulter, USA) in Sun Yat-Sen University Laboratory Animal Center. All data were expressed as mean ± standard deviation. For histological examination, the organs from various groups were fixed in 4% formalin and processed routinely into paraffin, sectioned into thin slices for H&E staining using standard techniques. The slices were examined under the Leica DMi1 microscope.

3. Results and discussion

3.1. Synthesis and characterization of BPQD/Cys-8E nanoparticles

The BPQDs were prepared by a liquid exfoliation technique reported
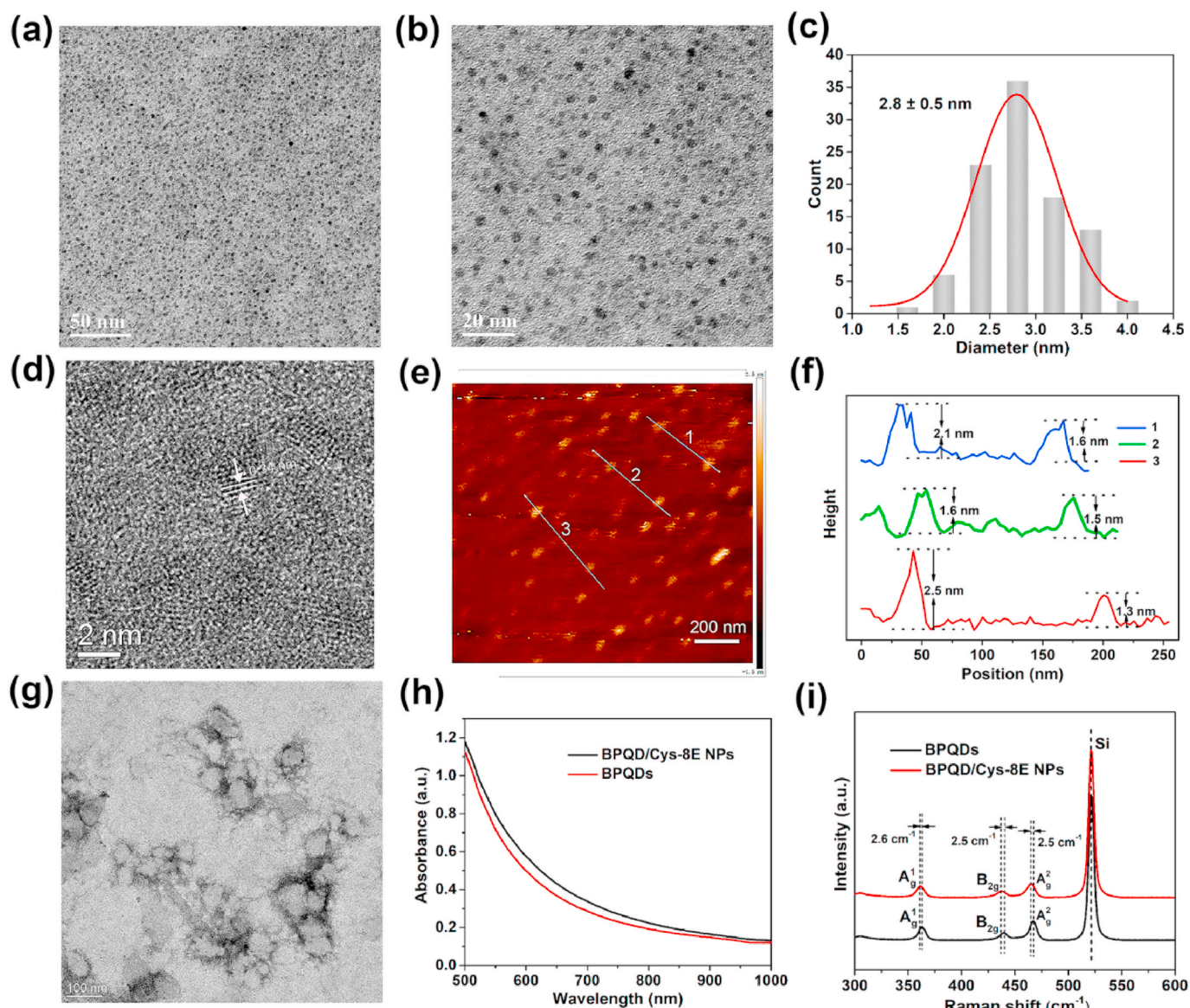
Fig. 1. Characterization of BPQDs and BPQD/Cys-8E NPs. TEM images of BPQDs (a) scale bar: 50 nm and (b) scale bar: 20 nm. (c) Statistical analysis of the sizes of 100 BPQDs based on the TEM images. (d) High-resolution TEM images of the BPQDs (scale bar: 1 nm). (e) AFM image of the BPQDs (scale bar: 2 nm). (f) Height profiles along the white lines in e. (g) TEM images of the BPQD/Cys-8E NPs (scale bar: 100 nm). (h) UV–vis–NIR spectra and (i) Raman spectra of BPQDs and BPQD/Cys-8E NPs deposited on a Si wafer.

previously [26]. Transmission electron microscopy (TEM) analysis (Fig. 1a) showed that BPQDs were relatively monodisperse with a lateral size of 2.8 ± 0.5 nm (Fig. 1c), which was acquired according to statistical TEM analysis of 100 BPQDs in Fig. 1b. The high-resolution TEM (HRTEM) image shows that the BPQDs were well crystallized with the lattice fringes of 0.34 nm (Fig. 1d), which are ascribed to the (021) plane of the BP crystal [28]. Furthermore, the thickness of the BPQDs was investigated by using atomic force microscopy. The atomic force microscopy (AFM) image (Fig. 1e and f) shows that BPQDs range from 1.3 to 2.5 nm in height, which corresponds to a stack of quintuple BP layers [29]. The high angle annular dark field scanning transmission electron microscopy (HAADF-STEM) image also shows the ultra-small and monodispersed morphologies of BPQDs (Fig. S1a). The UV–vis–NIR spectra of BPQDs and BPQD/Cys-8E NPs are displayed in Fig. 1h, both of which exhibited typical broad absorption bands from the UV to NIR regions, which are suitable for photothermal therapy. Furthermore, Raman scattering was also conducted to characterize the BPQDs. Both Raman spectra shown in Fig. 1i exhibit three obvious peaks correspond

to one out-of-plane phonon mode (A_g^1) and two in-plane modes (B_{2g}^2 and A_g^2), which demonstrates the crystalline features of BP nanostructures [30,31]. BPQD/Cys-8E NPs were synthesized by a nanoprecipitation method [32,33]. The morphologies of BPQD/Cys-8E NPs were investigated by TEM and HAADF-STEM analysis, which illustrated the nanosized vesicle-like structures (Fig. 1g and Fig. S1b). The loading efficiency and encapsulation efficiency were determined by inductively coupled plasma-mass spectrometry are 15.1% and 90.38%, respectively. When halving the amount of quantum dots, the encapsulation efficiency reached up to 97.8%. The dynamic light scattering data showed the size distribution of the BPQD/Cys-8E NPs was 155 nm (Fig. S2a), which falls within the suitable range for efficient uptake by tumor cells via the enhanced permeability and retention effect [34,35]. The potential of the BPQDs did not obviously change after modification with Cys-8E (Fig. S2b). The AFM image showed the height of BPQD/Cys-8E NPs (Fig. S3).
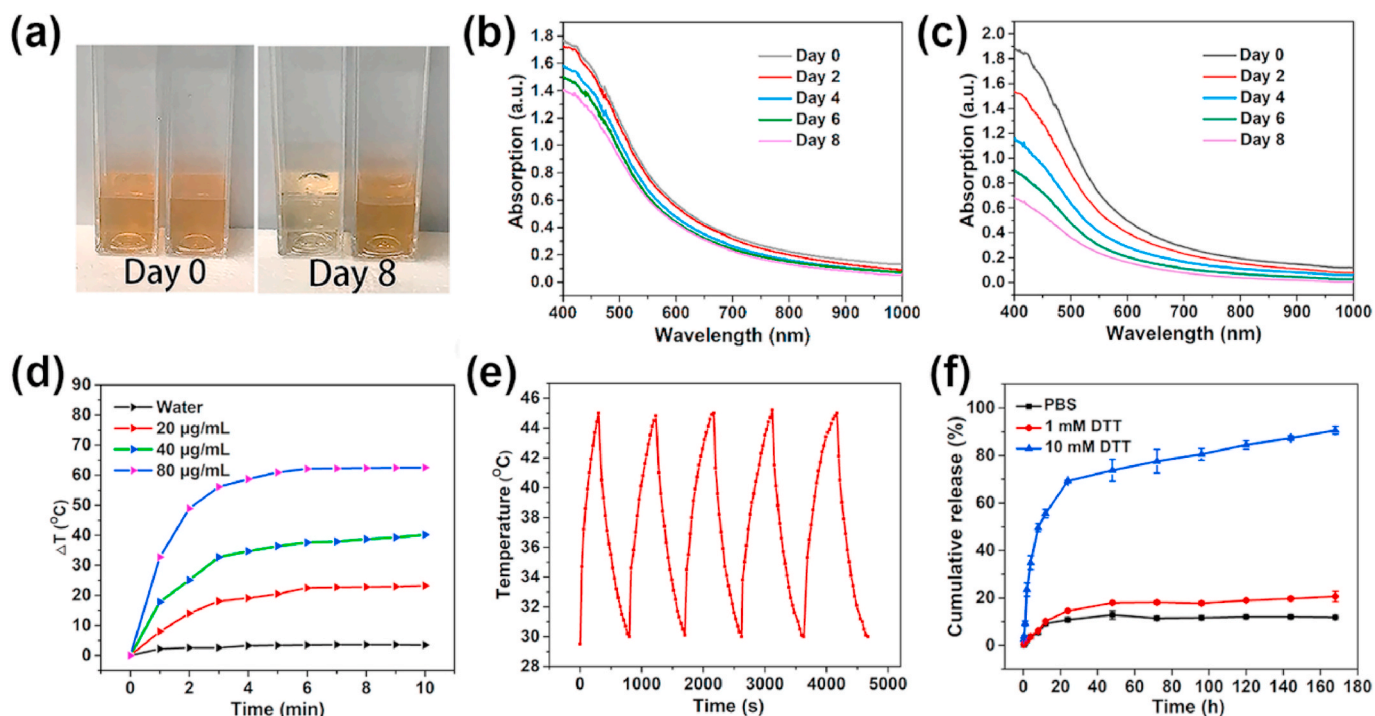
Fig. 2. (a) Photographs of BPQDs and BPQD/Cys-8E with the same amount of BPQDs (20 μg/mL) after storing in water at day 0 and day 8 (left: BPQDs and right: BPQD/Cys-8E). Ultraviolet–visible spectra of the (b) BPQD/Cys-8E NPs and (c) BPQDs with the concentration of 20 μg/mL after storing in water for different periods of time. (d) NIR-induced heat generation of different concentrations of BPQD/Cys-8E aqueous dispersion. (e) Temperature curves of BPQD/Cys-8E solution under five laser on/off cycles. (f) PTX release profiles of BPQD/Cys-8E/PTX measured by HPLC.

3.2. Stability of BPQD/Cys-8E nanoparticles

The BPQD/Cys-8E NPs and BPQDs aqueous solution or phosphate buffered saline (PBS) solution with the same amount of BPQDs were used to evaluate the stability of the samples (Fig. S4). Compared with bare BPQDs, the color and the near-infrared absorption at 808 nm of the BPQD/Cys-8E aqueous solution was almost the same during dispersion (Fig. 2a–c). The much better stability of BPQD/Cys-8E NPs was also confirmed (Fig. S5 and Fig. S6). These phenomena may have been due to the strong hydrophobicity inside Cys-8E protected the BPQDs from oxygen and water adequately leading to the excellent stability of the BPQD/Cys-8E NPs [21]. The near-infrared photo-absorption motivated us to evaluate the photothermal effect of BPQD/Cys-8E. Different concentrations of BPQD/Cys-8E aqueous solutions were exposed to a continuous-wave fiber-coupled diode 808 nm (2 W/cm^2) near-infrared laser for 10 min. Fig. 2d shows a concentration-dependent rapid temperature rise of BPQD/Cys-8E NPs, in which the temperature of the solution increased by 59 °C after 10 min when the concentration was 80 μg/mL. In contrast, the water only increased by 3.5 °C during the near-infrared irradiation. BPQD/Cys-8E NPs also demonstrated an excellent photothermal stability under five repeated five laser on/off cycles of near-infrared exposure (Fig. 2e). The photothermal conversion efficiency of BPQD/Cys-8E NPs was calculated to be 39.9% according to the literature (Fig. S7) [36].

3.3. Photothermal optical coherence tomography

The fascinating photothermal feature impelled us to conduct the PT-OCT bio-imaging using BPQD/Cys-8E NPs as the novel photothermal-responsive nanoagents, which has never been reported before. A PT-OCT imaging system with an axial resolution of 13.8 μm and lateral resolution of 17.5 μm was developed as illustrated in Fig. 3a, where a super luminescent diode (1310 nm) and a pump laser (532 nm) were equipped as the OCT light source and photothermal excitation light, respectively. Fig. 3b shows the PT-OCT images obtained from the 2%

(w/v) agarose gel containing BPQDs with the concentrations of 0, 6.25, 12.5, 25, 50 and 100 μg/mL, respectively. Clearly, the PT-OCT signals increased with the increasing BPQDs concentrations in agarose gel, and fit well with the linear model (R^2 = 0.985; Fig. S8), showing a linear relationship between the PT-OCT intensity and the nanoparticle concentration ranged from 0 to 100 μg/mL. Then, 4T1 breast tumor-bearing BALB/c mouse model was established to investigate the *in vivo* PT-OCT imaging capability of BPQD/Cys-8E NPs. Nanoparticles were intravenously injected into the mice, and then the animals were placed in the system for PT-OCT imaging at different time points. Fig. 3c exhibits the typical PT-OCT B-scans of tumor tissues at 0, 8, 12, 24 and 48 h, and the green regions represent the photothermal signals inside the tissues. Time-dependent tumor uptake of nanoparticles was observed, and the most intense signals appeared at 24 h after injection, which may be ascribed to the maximal accumulation of BPQD/Cys-8E NPs in tumors. Afterward, reconstructed 3D PT-OCT images of the scanning regions (~3 × 3 mm) were obtained from 500 consecutive B-scans, which enabled us to estimate the stereoscopic distribution of nanomaterials in the tumor (Fig. 3d and Fig. S9). Fig. 3e depicts the top views of 3D PT-OCT images of tumors at various time points after BPQD/Cys-8E NPs injection. At 0 h, only a vague image was observed with low contrast (Fig. S9). With the increase of cycle time, the microstructures of tumor tissues became more unambiguous until 24 h. More interestingly, we could clearly observe the microvessels from the PT-OCT image of tumor tissue at 24 h, which revealed that the nanosystem largely accumulated in the tumor microenvironment. The data exemplified above greatly supported the promising potential of BPQD/Cys-8E NPs for PT-OCT bio-imaging.

3.4. In vitro cancer therapeutic efficacy

The safety of BPQD/Cys-8E NPs in human liver hepatocellular carcinoma (HepG2) human non-small cell lung cancer (H1650) cells, mouse fibroblast (NIH 3T3) cells and murine breast cancer (4T1) cells were investigated by the a cell counting kit-8 (CCK-8) assay, which
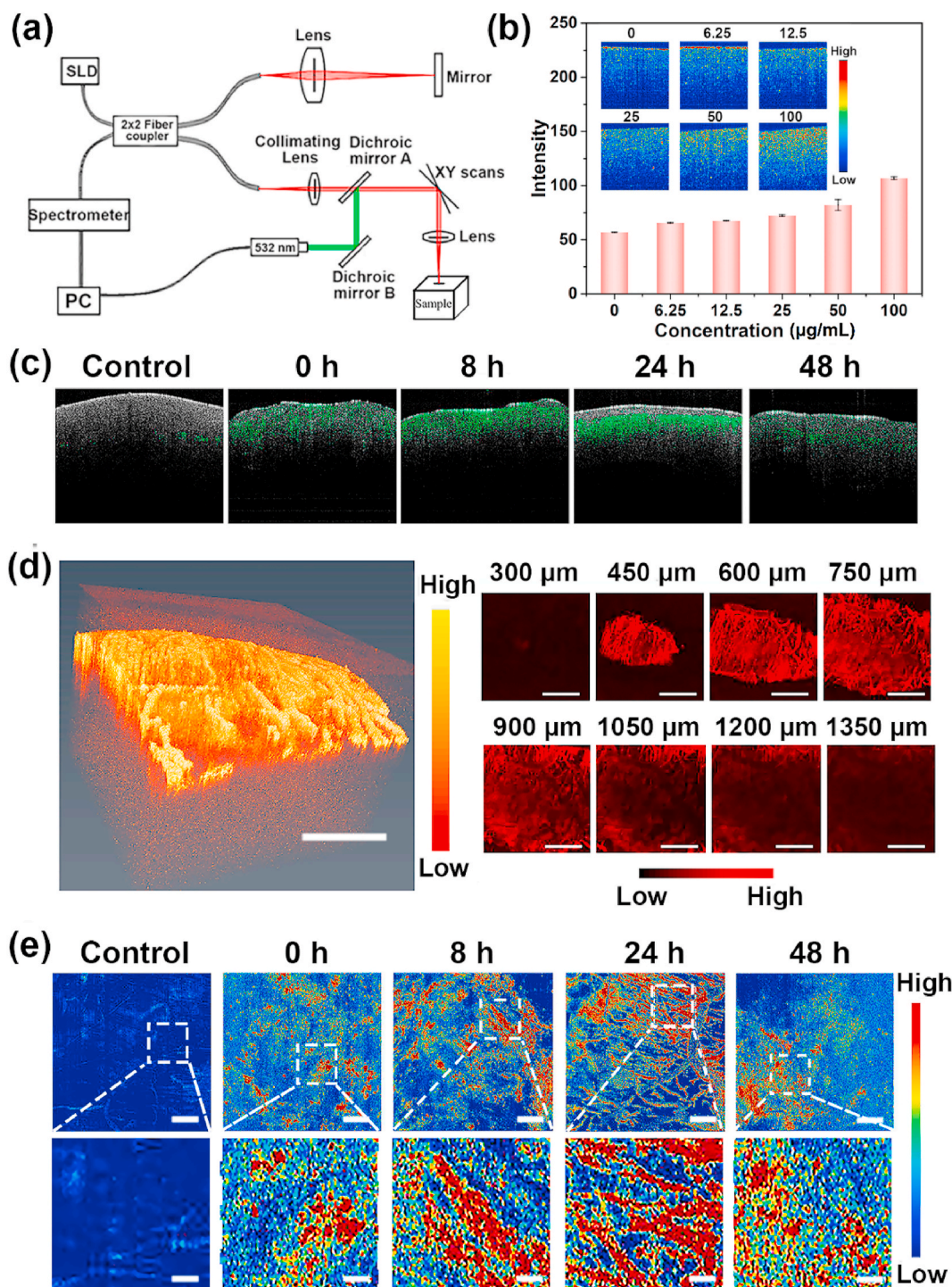
Fig. 3. Photothermal OCT imaging based on BPQD/Cys-8E NPs. (a) Schematic diagram of the PT-OCT system. (b) PT-OCT B-scans of 2% (w/v) agarose gel containing different concentrations of BPQD/Cys-8E NPs. (c) Typical PT-OCT B-scans of mice tumors injected with BPQD/Cys-8E NPs captured at 0, 8, 12, 24 and 48 h. (d) 3D PT-OCT image of tumor with BPQD/Cys-8E NPs at 24 h post-injection and corresponding cross-sectional PT-OCT images obtained at different depths (300, 450, 600, 750, 900, 1050, 1200 and 1350 μm) of tumor injected with BPQD/Cys-8E NPs at 24 h (scale bars: 1 mm). (e) The top views of 3D PT-OCT images of tumor regions (~3 × 3 mm) reconstructed from 500 consecutive B-scans (scale bars: 1 mm).

revealed no obvious toxic effects on both types of cells as much as at internal BPQDs concentration up to 100 μg/mL (Fig. 4a). Flow cytometry analysis confirmed that the behavior of coumarin 6 (C6) labeled Cys-8E NPs entered into tumor cells was time dependent (Fig. S10). Then, Dil-labeled BPQD/Cys-8E NPs were co-incubated with lysosome marker (Lysotracker Green) to study the intracellular trafficking and intracellular localization of nanomaterials in HepG2 cells. As displayed in the confocal microscopy images (Fig. 4b), obvious red fluorescence signals were observed, which revealed the effective uptake of BPQD/Cys-8E NPs by HepG2 cells. The overlap of green and red fluorescence signals reached the a maximum at 2 h then declined at 4 h, which indicated the endocytosis of BPQD/Cys-8E NPs inside cells complies with the lysosome pathway. Afterward, BPQD/Cys-8E NPs were loaded with an anti-tumor drug (PTX) to facilitate the chemotherapy and photothermal tumor therapy.

The Cys-8E platform demonstrated good drug loading efficiency and
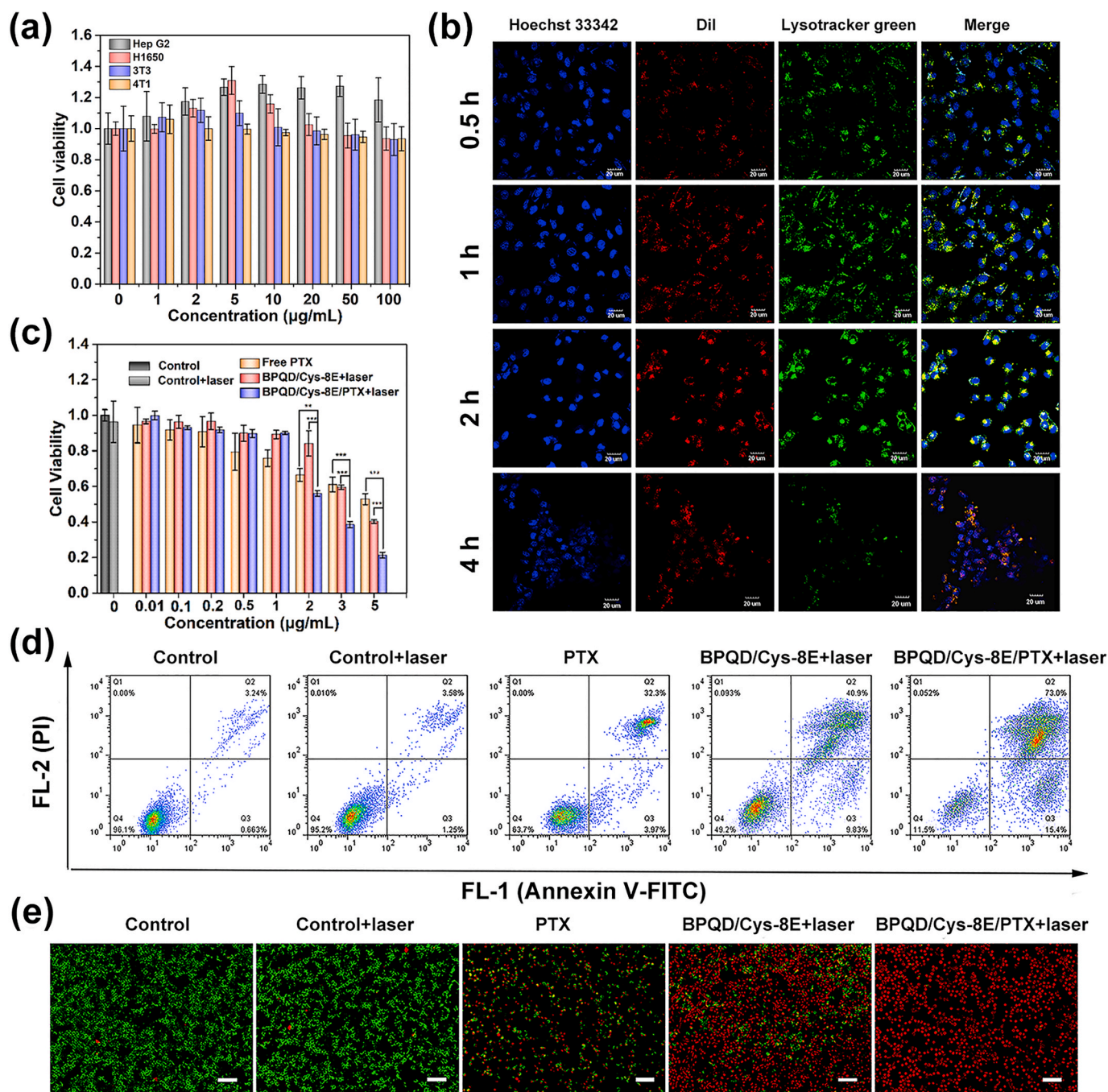
Fig. 4. In *vitro* antitumor effect of BPQD/Cys-8E NPs. (a) Relative viabilities of HepG2 cells, H1650 cells, NIH-3T3 cells and 4T1 cells after incubation with BPQD/Cys-8E NPs (internal BPQDs concentrations of 0, 2, 5, 10, 20, 50 and 100 μg/mL) for 24 h. (b) Confocal microscopy images of HepG2 cells incubated with DiI-labeled BPQD/Cys-8E NPs for 0.5, 1, 2, and 4 h (scale bars: 20 μm). (c) Relative viability of HepG2 cells after various treatments. (d) Flow cytometry studies of HepG2 cells after various treatments for 24 h. (e) Fluorescence images (scale bars: 100 μm) of the cells stained with calcein AM (live cells, green fluorescence) and PI (dead cells, red fluorescence).

sensitive GSH-responsive PTX release (Fig. 2f). We selected the ratio of Cys-8E/BPQD/PTX = 20:2:1 with the highest encapsulation efficiency (95% for BPQD and 40% for PTX) and drug loading efficiency (23.75% for BPQD and 5% for PTX) in our following study. HepG2 cells and 4T1 cells were irradiated with the 808 nm laser (2 W/cm^2) for 3 min after incubation with nanoparticles for 4 h, and then, the cellular viability was investigated by a CCK-8 assay. A dose-dependent anti-cancer effect can be observed in Fig. 4c and Fig. S11, and the cells viability of the cells in the laser only group was not compromise the cell viability. Among all, the cancer cells underwent photothermal therapy and drug

treatment maintained the minimal cell population, which shows a good synergistic effect between the two treatments. The chemo-photothermal combined therapeutic effect of the BPQD/Cys-8E/PTX NPs was also confirmed by the flow cytometry analysis at the same drug concentration and irradiation time for 12 h (Fig. S12) and 24 h (Fig. 4d). In addition, HepG2 cells were co-stained with calcein AM (live cells, green fluorescence) and propidium iodide (PI, dead cells, red fluorescence) after various treatments. As shown in Fig. 4e, the cell ablation effect of BPQD/Cys-8E is significantly improved by near-infrared laser irradiation or PTX exposure and the tumor suppressive effect reached a peak in
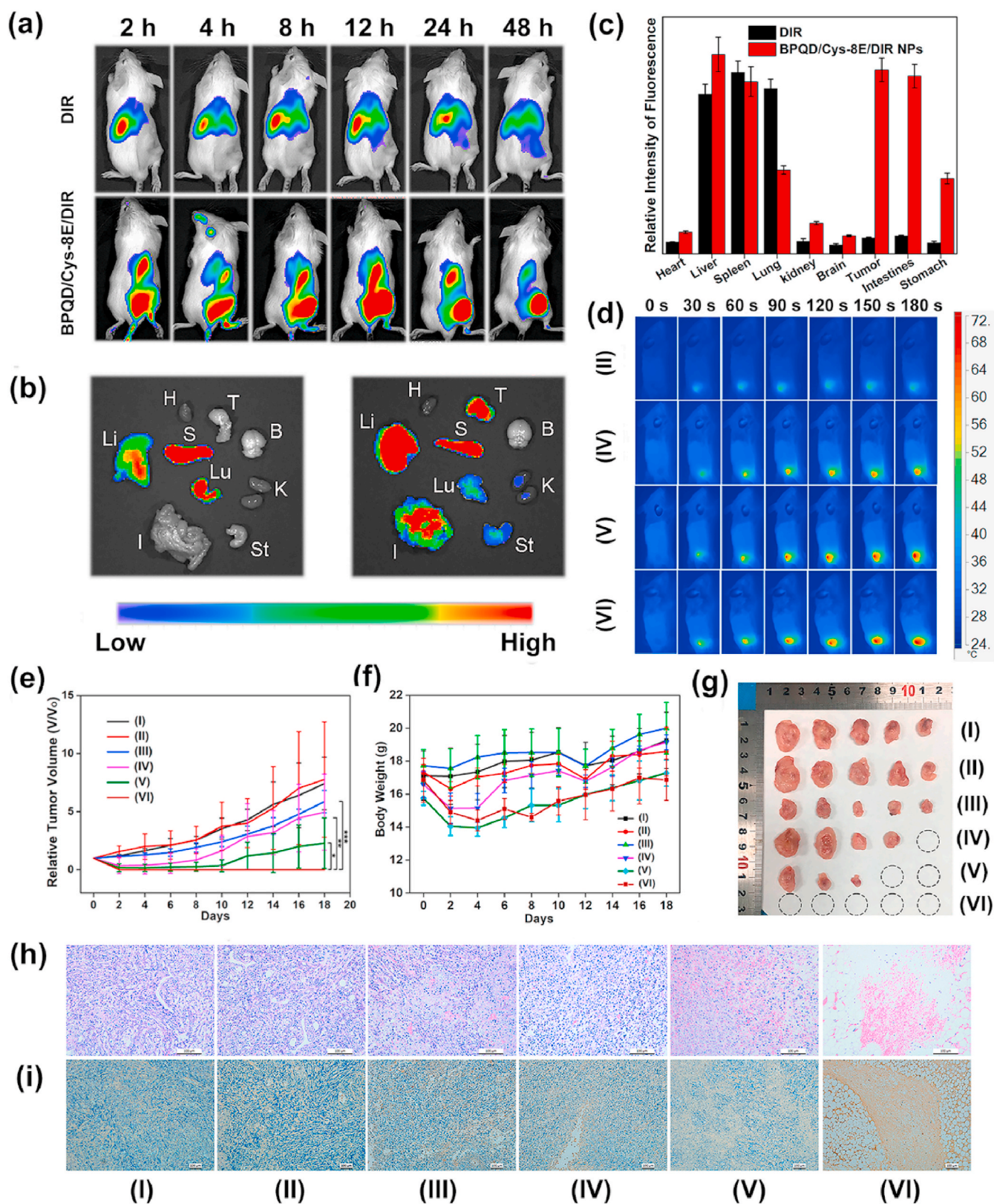
Fig. 5. *In vivo* antitumor experiments. (a) Near-infrared fluorescence (NIRF) imaging of mice injected with free DiR and DiR-labeled BPQD/Cys-8E NPs at different time points. (b) NIRF imaging and (c) corresponding fluorescence quantitative assessment of major organs and tumors extracted from mice at 48 h post-injection. H, heart; Li, liver; Sp, spleen; Lu, lung; K, kidney; B, brain; I, intestine; St, stomach; T, tumor. (d) Infrared thermal images of 4T1-tumor-bear mice under near-infrared laser irradiation. (e) Tumor growth curves of mice after treatment (Group I: control, Group II: control + laser, Group III: PTX, Group IV: BPQDs, Group V: BPQD/Cys-8E + laser, Group VI: BPQD/Cys-8E/PTX + laser). (f) Mean body weights of mice in various groups. (g) Photographs of the tumors collected from different groups of mice at the end of treatments (day 18). Representative (h) H&E-stained and (i) TUNEL-stained tumor slice images from mice post various treatments (scale bars: 100 μm).

the combined group, where almost all cancer cells were killed after incubation with BPQD/Cys-8E/PTX plus an near-infrared laser.

3.5. In vivo cancer therapeutic efficacy

For *in vivo* biomedical application, the *in vivo* behavior of the BPQD/Cys-8E NPs was first investigated by using a near-infrared whole animal imaging system. Near-infrared fluorescence (NIRF) dye DiR-labeled BPQD/Cys-8E NPs were systemically administered into mice via tail vein injection, and then, the NIRF images of mice were captured at various times. As shown in Fig. 5a, the fluorescence signals of BPQD/Cys-8E NPs were easily observed at the tumor site as early as 2 h post injection, which indicated a rapid tumor accumulation of the nanosystem mediated by Cys-8E vesicles. The fluorescence intensity in the tumor gradually increased and still maintained strong fluorescence at 24 h post injection, which suggests good retention of BPQD/Cys-8E NPs in the tumor tissue. In contrast, mice injected with free DiR only emitted weak fluorescence and few signals were observed in the tumor site. Fig. 5b illustrates the NIRF images of excised organs of mice 48 h after systemic injection of free DiR and DiR-labeled BPQD/Cys-8E NPs, respectively. The fluorescence signals of liver and spleen were seen in both groups may be due to reticuloendothelial system absorption of fluorophore [37]. In addition, the NIRF signals of tumor tissue containing DiR-labeled BPQD/Cys-8E NPs were significantly higher than that of mice injected with free DiR (Fig. 5c), which may be attributed to the excellent tumor accumulation capability of the nanosystem [38].

Thereafter, *in vivo* chemo-photothermal antitumor experiments based on BPQD/Cys-8E/PTX NPs were performed. A volume of 100 μL PBS, PTX, BPQDs, BPQD/Cys-8E and BPQD/Cys-8E/PTX NPs were injected separately into mice via tail veins before near-infrared irradiation. An infrared thermal camera was used to monitor the real-time temperature change *in vivo*. As displayed in Fig. 5d, the tumor sites in mice treated with bare BPQDs (Groups VI), increased by only 10.3 °C which was only just slightly higher than that of mice injected with PBS (Group II, 5.5 °C). In contrast, the mice injected with the BPQD/Cys-8E and BPQD/Cys-8E/PTX exhibited remarkable temperature increases within 3 min ($\Delta T \approx 30$ °C) under the near-infrared irradiation and the maximum temperature reached 64 °C, which is high enough for tumor ablation [39], indicates the excellent photothermal efficiency of Cys-8E encapsulated BPQDs as the photothermal therapy agent for *in vivo* tumor ablation. The combined *in vivo* therapeutic efficacies were evaluated by detecting the tumor sizes using a digital caliper. The relative tumor volume curves after various treatments are shown in Fig. 5e. An optimal *in vivo* anti-tumor effect is observed in the BPQD/Cys-8E/PTX + laser group, where the tumors of the mice shrink gradually, then are completely cured with only black scabs were left; more importantly, no recurrence was observed (Fig. 5g and Fig. S13). However, the tumors of mice in Groups I and II experienced rapid growth during the 18-day observation period. The tumors of mice treated with PTX experience an equivalent growth rate in comparison with that of the control groups, which demonstrates that the dosage of administered PTX was inadequate to inhibit the tumor growth. Regarding the mice treated with bare BPQDs, the tumor growth was not inhibited effectively, which may have been due to the partial degradation of bare BPQDs during *in vivo* delivery process. The tumors in Group V were effectively eliminated initially, but relapsed to some extent, due to the incomplete ablation of tumor cells.

The effect of chemo-photothermal treatment was also analyzed by the hematoxylin and eosin (H&E) staining and a terminal deoxynucleotidyl transferase-mediated deoxyuridine triphosphate nick end-labeling (TUNEL) assay (Fig. 5i). Fig. 5h shows the H&E stained microscopic images of tumors collected 1 day post treatment. It can obviously be seen that the cellular architectures of tumor tissues in Group VI were severely damaged, while the tumors in the control groups maintained densely neoplastic cells with regular morphologies and intact cell nuclei [40,41]. The TUNEL assay (Fig. 5i) revealed a spot of

TUNEL-positive cells (dead cells, brown color) in the free PTX and BPQDs + laser groups. However, the dead cells became evident after the mice underwent chemotherapy or photothermal therapy, and the largest population of TUNEL-positive cells was discovered in the BPQD/Cys-8E/PTX + laser group, which uncovered the synergistic effect of chemo-photothermal tumor therapy [42,43].

To determine whether there were toxic adverse effects for the black phosphorus-based theranostic platform, the body weight of the mice was monitored every other day. As shown in Fig. 5f, no significant body weight loss was seen during the 18-day observation period. Next, the H&E staining of major organs including heart, liver, kidney, lung and spleen harvested from all the treated groups at 18 days showed no indication of inflammation, cell necrosis, or apoptosis (Fig. S14). In addition, blood biochemical analyses were conducted, and various markers, including alanine transaminase (ALT), aspartate transaminase (AST), globulin (GLB), total protein (TP), albumin/globin ratio (A/G), total bilirubin (TBIL), blood urea nitrogen (BUN), creatinine (CREA) and albumin (ALB) were examined, which showed no significant changes in the blood chemistry of mice (Fig. S15). As the ALT, AST, ALP, ALB and TP levels are usually closely associated with the functions of the liver and kidney of mice, while CREA and BUN relate to the function of the kidney [44], the results confirm that the treatment does not cause obvious hepatic or renal toxicity [45,46].

4. Conclusion

In conclusion, a biodegradable black phosphorus-based theranostic platform (BPQD/Cys-8E NPs) was successfully developed. The stability and near-infrared photothermal performance of the BPQDs in the physiological environment were significantly improved due to protection of Cys-8E. The excellent photothermal feature allows BPQD/Cys-8E NPs to serve as a novel contrast agent for high-resolution PT-OCT bioimaging. Furthermore, BPQD/Cys-8E NPs could responsive to redox changes, leading to more PTX/BPQDs release in tumor tissues. Combined with the superior photothermal therapy effect, high-performance chemo-photothermal cancer therapy has been accomplished with very low PTX dosage *in vitro* and *in vivo*. In addition, no toxicity was observed from the BPQDs-based theranostic platform, indicating the excellent biocompatibility. This study provides an example of a completely biodegradable nanoagent for PT-OCT bio-imaging and chemo-photothermal cancer therapy, indicating the great potential of black phosphorus-based platform for cancer theranostics.

CRediT authorship contribution statement

Haolin Chen: Conceptualization, Methodology, Investigation, Formal analysis, Writing - original draft. **Zhiming Liu:** Conceptualization, Investigation, Methodology, Funding acquisition, Writing - review & editing. **Bo Wei:** Formal analysis, Resources, Validation. **Jun Huang:** Methodology, Resources, Validation, Funding acquisition. **Xinru You:** Investigation, Validation. **Jingyang Zhang:** Investigation. **Zhiling Yuan:** Resources. **Zhilie Tang:** Validation. **Zhouyi Guo:** Validation. **Jun Wu:** Conceptualization, Supervision, Project administration, Funding acquisition, Writing - review & editing.

Declaration of competing interest

The authors declare that they have no known competing financial interests or personal relationships that could have appeared to influence the work reported in this paper.

Acknowledgements

Appendix A. Supplementary data

Supplementary data to this article can be found online at https://doi.org/10.1016/j.bioactmat.2020.08.034.

References

[1] S. Kunjachan, J. Ehling, G. Storm, F. Kiessling, T. Lammers, Noninvasive imaging of nanomedicines and nanotheranostics: principles, progress, and prospects, Chem. Rev. 115 (2015) 10907–10937.

[2] Y. Liu, P. Bhattarai, Z. Dai, X. Chen, Photothermal therapy and photoacoustic imaging via nanotheranostics in fighting cancer, Chem. Soc. Rev. 48 (2019) 2053–2108.

[3] N. Jailkhani, J.R. Ingram, M. Rashidian, S. Rickelt, C. Tian, H. Mak, Z. Jiang, H.L. Ploegh, R.O. Hynes, Noninvasive imaging of tumor progression, metastasis, and fibrosis using a nanobody targeting the extracellular matrix, Proc. Natl. Acad. Sci. U.S.A. 116 (2019) 14181–14190.

[4] K.D. Bojikian, P.P. Chen, J.C. Wen, Optical coherence tomography angiography in glaucoma, Curr. Opin. Ophthalmol. 30 (2019) 110–116.

[5] M. Liu, W. Drexler, Optical coherence tomography angiography and photoacoustic imaging in dermatology, Photochem. Photobiol. Sci. 18 (2019) 945–962.

[6] C. Ung, J.B. Miller, Intraoperative optical coherence tomography in vitreoretinal surgery, Semin. Ophthalmol. 34 (2019) 312–316.

[7] M. Lapierre-Landry, A.L. Huckenpahler, B.A. Link, R.F. Collery, J. Carroll, M.C. Skala, Imaging melanin distribution in the zebrafish retina using photothermal optical coherence nomography, Transl. Vis Sci. Technol. 7 (2018) 4.

[8] D.C. Adler, S.-W. Huang, R. Huber, J.G. Fujimoto, Photothermal detection of gold nanoparticles using phase-sensitive optical coherence tomography, Optic Express 16 (2008) 4376–4393.

[9] A.Y. Gordon, M. Lapierre-Landry, M.C. Skala, J.S. Penn, Photothermal optical coherence tomography of anti-angiogenic treatment in the mouse retina using gold nanorods as contrast agents, Transl. Vis Sci. Technol. 8 (2019) 18.

[10] M.C. Skala, M.J. Crow, A. Wax, J.A. Izatt, Photothermal optical coherence tomography of epidermal growth factor receptor in live cells using immunotargeted gold nanospheres, Nano Lett. 8 (2008) 3461–3467.

[11] Y. Jung, R. Reif, Y. Zeng, R.K. Wang, Three-dimensional high-resolution imaging of gold nanorods uptake in sentinel lymph nodes, Nano Lett. 11 (2011) 2938–2943.

[12] A.L. Oldenburg, M.N. Hansen, D.A. Zweifel, A. Wei, S.A. Boppart, Plasmon-resonant gold nanorods as low backscattering albedo contrast agents for optical coherence tomography, Optic Express 14 (2006) 6724–6738.

[13] N. Khlebtsov, L. Dykman, Biodistribution and toxicity of engineered gold nanoparticles: a review of in vitro and in vivo studies, Chem. Soc. Rev. 40 (2011) 1647–1671.

[14] A. Hirsch, F. Hauke, Post-graphene 2D chemistry: the emerging field of molybdenum disulfide and black phosphorus functionalization, Angew. Chem. Int. Ed. 57 (2018) 4338–4354.

[15] X. Ling, H. Wang, S. Huang, F. Xia, M.S. Dresselhaus, The renaissance of black phosphorus, Proc. Natl. Acad. Sci. U.S.A. 112 (2015) 4523–4530.

[16] W. Tao, N. Kong, X. Ji, Y. Zhang, A. Sharma, J. Ouyang, B. Qi, J. Wang, N. Xie, C. Kang, H. Zhang, O.C. Farokhzad, J.S. Kim, Emerging two-dimensional monoelemental materials (Xenes) for biomedical applications, Chem. Soc. Rev. 48 (2019) 2891–2912.

[17] Y. Li, Z. Liu, Y. Hou, G. Yang, X. Fei, H. Zhao, Y. Guo, C. Su, Z. Wang, H. Zhong, Z. Zhuang, Z. Guo, Multifunctional nanoplatform based on black phosphorus quantum dots for bioimaging and photodynamic/photothermal synergistic cancer therapy, ACS Appl. Mater. Interfaces 9 (2017) 25098–25106.

[18] W. Tao, X. Zhu, X. Yu, X. Zeng, Q. Xiao, X. Zhang, X. Ji, X. Wang, J. Shi, H. Zhang, Black phosphorus nanosheets as a robust delivery platform for cancer theranostics, Adv. Mater. 29 (2017) 1603276.

[19] X. Yang, D. Wang, J. Zhu, L. Xue, C. Ou, W. Wang, M. Lu, X. Song, X. Dong, Functional black phosphorus nanosheets for mitochondria-targeting photothermal/photodynamic synergistic cancer therapy, Chem. Sci. 10 (2019) 3779–3785.

[20] X. Yang, G. Liu, Y. Shi, W. Huang, J. Shao, X. Dong, Nano-black phosphorus for combined cancer phototherapy: recent advances and prospects, Nanotechnology 29 (2018) 222001.

[21] J. Shao, H. Xie, H. Huang, Z. Li, Z. Sun, Y. Xu, Q. Xiao, X.F. Yu, Y. Zhao, H. Zhang, H. Wang, P.K. Chu, Biodegradable black phosphorus-based nanospheres for in vivo photothermal cancer therapy, Nat. Commun. 7 (2016) 12967.

[22] Z. Tang, N. Kong, J. Ouyang, C. Feng, N.Y. Kim, X. Ji, C. Wang, O.C. Farokhzad,

[23] H. Zhang, W. Tao, Phosphorus science-oriented design and synthesis of multifunctional nanomaterials for biomedical applications, Matter 2 (2020) 297–322.

[23] N. Kong, X. Ji, J. Wang, X. Sun, G. Chen, T. Fan, W. Liang, H. Zhang, A. Xie, O.C. Farokhzad, W. Tao, ROS-mediated selective killing effect of black phosphorus: mechanistic understanding and its guidance for safe biomedical applications, Nano Lett. 20 (2020) 3943–3955.

[24] L. Cheng, Z. Cai, J. Zhao, F. Wang, M. Lu, L. Deng, W. Cui, Black phosphorus-based 2D materials for bone therapy, Bioact. Mater. 5 (2020) 1026–1043.

[25] Z. Sun, Y. Zhao, Z. Li, H. Cui, Y. Zhou, W. Li, W. Tao, H. Zhang, H. Wang, P.K. Chu, X.F. Yu, TiL$_4$-coordinated black phosphorus quantum dots as an efficient contrast agent for in vivo photoacoustic imaging of cancer, Small 13 (2017) 1602896.

[26] Z. Sun, H. Xie, S. Tang, X.F. Yu, Z. Guo, J. Shao, H. Zhang, H. Huang, H. Wang, P.K. Chu, Ultrasmall black phosphorus quantum dots: synthesis and use as photothermal agents, Angew. Chem. Int. Ed. 54 (2015) 11526–11530.

[27] H. Zhang, T. Fan, W. Chen, Y. Li, B. Wang, Recent advances of two-dimensional materials in smart drug delivery nano-systems, Bioact. Mater. 5 (2020) 1071–1086.

[28] P. Yasaei, B. Kumar, T. Foroozan, C. Wang, M. Asadi, D. Tuschel, J.E. Indacochea, R.F. Klie, A. Salehi-Khojin, High-quality black phosphorus atomic layers by liquid-phase exfoliation, Adv. Mater. 27 (2015) 1887–1892.

[29] X. Zhang, H. Xie, Z. Liu, C. Tan, Z. Luo, H. Li, J. Lin, L. Sun, W. Chen, Z. Xu, L. Xie, W. Huang, H. Zhang, Black phosphorus quantum dots, Angew. Chem. Int. Ed. 54 (2015) 3653–3657.

[30] S. Zhang, X. Zhang, W. Hao, B. Chen, W. Kan, K. Wang, D. Hanlon, J.N. Coleman, J. Chen, Z. Long, Size-dependent saturable absorption and mode-locking of dispersed black phosphorus nanosheets, Opt. Mater. Express 9 (2016) 372–377.

[31] H. Wang, X. Yang, W. Shao, S. Chen, J. Xie, X. Zhang, J. Wang, Y. Xie, Ultrathin black phosphorus nanosheets for efficient singlet oxygen generation, J. Am. Chem. Soc. 137 (2015) 11376–11382.

[32] X. Ling, X. Chen, I.A. Riddell, W. Tao, J. Wang, G. Hollett, S.J. Lippard, O.C. Farokhzad, J. Shi, J. Wu, Glutathione-scavenging poly(disulfide amide) nanoparticles for the effective delivery of Pt (IV) prodrugs and reversal of cisplatin resistance, Nano Lett. 18 (2018) 4618–4625.

[33] J. Wu, L. Zhao, X. Xu, N. Bertrand, W.I. Choi, B. Yameen, J. Shi, V. Shah, M. Mulvale, J.L. MacLean, O.C. Farokhzad, Hydrophobic cysteine poly(disulfide)-based redox-hypersensitive nanoparticle platform for cancer theranostics, Angew. Chem. Int. Ed. 54 (2015) 9218–9823.

[34] J.S. Kim, K.J. Cho, T.H. Tran, M. Nurunnabi, T.H. Moon, S.M. Hong, Y.K. Lee, In vivo NIR imaging with CdTe/CdSe quantum dots entrapped in PLGA nanospheres, J. Colloid Interface Sci. 353 (2011) 363–371.

[35] E.I. Altinoglu, T.J. Russin, J.M. Kaiser, B.M. Barth, P.C. Eklund, M. Kester, J.H. Adair, Near-infrared emitting fluorophore-doped calcium phosphate nanoparticles for in vivo imaging of human breast cancer, ACS Nano 2 (2008) 2075–2084.

[36] K. Hu, L. Xie, Y. Zhang, M. Hanyu, Z. Yang, K. Nagatsu, H. Suzuki, J. Ouyang, X. Ji, J. Wei, H. Xu, O.C. Farokhzad, S.H. Liang, L. Wang, W. Tao, M.-R. Zhang, Marriage of black phosphorus and Cu2 + as effective photothermal agents for PET-guided combination cancer therapy, Nat. Commun. 11 (2020) 2778.

[37] N.T. Huynh, E. Roger, N. Lautram, J.P. Benoit, C. Passirani, The rise and rise of stealth nanocarriers for cancer therapy: passive versus active targeting, Nanomedicine 5 (2010) 1415–1433.

[38] L. Cheng, C. Wang, L. Feng, K. Yang, Z. Liu, Functional nanomaterials for photo-therapies of cancer, Chem. Rev. 114 (2014) 10869–10939.

[39] P. Yang, S. Zhang, N. Zhang, Y. Wang, J. Zhong, X. Sun, Y. Qi, X. Chen, Z. Li, Y. Li, Tailoring synthetic melanin nanoparticles for enhanced photothermal therapy, ACS Appl. Mater. Interfaces 11 (2019) 42671–42679.

[40] C. Huang, Z. Sun, H. Cui, T. Pan, S. Geng, W. Zhou, P.K. Chu, X.F. Yu, InSe nanosheets for efficient NIR-II-Responsive drug release, ACS Appl. Mater. Interfaces 11 (2019) 27521–27528.

[41] Q. Yu, Y. Han, X. Wang, C. Qin, D. Zhai, Z. Yi, J. Chang, Y. Xiao, C. Wu, Copper silicate hollow microspheres-incorporated scaffolds for chemo-photothermal therapy of melanoma and tissue healing, ACS Nano 12 (2018) 2695–2707.

[42] N. Kong, W. Tao, X. Ling, J. Wang, Y. Xiao, S. Shi, X. Ji, A. Shajii, S.T. Gan, N.Y. Kim, D.G. Duda, T. Xie, O.C. Farokhzad, J. Shi, Synthetic mRNA nanoparticle-mediated restoration of p53 tumor suppressor sensitizes p53-deficient cancers to mTOR inhibition, Sci. Transl. Med. 11 (2019) eaaw1565.

[43] Z. Chai, D. Ran, L. Lu, C. Zhan, H. Ruan, X. Hu, C. Xie, K. Jiang, J. Li, J. Zhou, J. Wang, Y. Zhang, R.H. Fang, L. Zhang, W. Lu, Ligand-modified cell membrane enables the targeted delivery of drug nanocrystals to glioma, ACS Nano 13 (2019) 5591–5601.

[44] X.D. Zhang, J. Chen, Y. Min, G.B. Park, X. Shen, S.-S. Song, Y.-M. Sun, H. Wang, W. Long, J. Xie, K. Gao, L. Zhang, S. Fan, F. Fan, U. Jeong, Metabolizable Bi2Se3 nanoplates: biodistribution, toxicity, and uses for cancer radiation therapy and imaging, Adv. Funct. Mater. 24 (2014) 1718–1729.

[45] J. Jiang, N. Shen, T. Ci, Z. Tang, Z. Gu, G. Li, X. Chen, Combretastatin A4 nanodrug-induced MMP9 amplification boosts tumor-selective release of doxorubicin prodrug, Adv. Mater. 31 (2019) e1904278.

[46] J. Ouyang, C. Feng, X. Ji, L. Li, H.K. Gutti, N.Y. Kim, D. Artzi, A. Xie, N. Kong, Y.N. Liu, G.J. Tearney, X. Sui, W. Tao, O.C. Farokhzad, 2D Monoelemental germanene quantum dots: synthesis as robust photothermal agents for photonic cancer nanomedicine, Angew. Chem. Int. Ed. 58 (2019) 13405–13410.